ROYAL SOCIETY
OF CHEMISTRY

PAPER

Check for updates

Regulating NO$_2$ adsorption at ambient temperature by manipulating copper species as binding sites in copper-modified SSZ-13 zeolites†

Mingzhe Sun,‡[ab] Tianqi Wang, ‡[ab] Calvin Ku,[a] Aamir Hanif,[ab] Tian Tian,[c] Bernt Johannessen,[de] Qinfen Gu, *[d] Ziyi Li, *[f] Patrick Sit *[a] and Jin Shang *[abg]

Atmospheric NO$_2$ pollution poses significant risks to human health and the environment even at low concentrations, necessitating the development of efficient technologies for its removal under ambient conditions. In this study copper (Cu)-modified SSZ-13 zeolites (referred to as Cu^{n+}SSZ-13 where n represents the valence state of Cu) were developed for NO$_2$ removal by adsorption. Cu^{n+}SSZ-13 zeolites containing Cu species with different valence states and proportions were prepared by reducing a Cu^{2+}-exchanged SSZ-13 zeolite (Cu^{2+}SSZ-13) using H$_2$ at different temperatures. The Cu^{n+}SSZ-13 reduced at 190 °C showed the highest NO$_2$ removal capacity (1.79 mmol g^{-1}), outperforming pristine SSZ-13 and Cu^{2+}SSZ-13 by 52.3% and 19.4%, respectively. The improvement was due to the increased amount of adsorption sites (Cu$^+$ and H$^+$) and the stronger affinity of Cu$^+$ than Cu^{2+} for NO$_2$, as confirmed by density functional theory (DFT) calculations. The generation of Cu^0 nanoparticles and moisture in zeolites during reduction was undesirable for NO$_2$ adsorption. However, this could be eliminated by lowering the reduction temperature and performing thermal activation, respectively. This work provides systematic methods for designing zeolite adsorbents for ambient NO$_2$ removal and offers insights into the burgeoning field of air pollution control.

1. Introduction

Nitrogen oxides (NO$_x$), including NO and NO$_2$, are primarily emitted from mobile and stationary sources such as vehicles and industries. NO$_x$ have raised public concerns due to their detrimental effects on both human health and ecosystems.[1–3] For example, NO$_x$ can interact with other air pollutants such as volatile organic compounds (VOCs) under sunlight, leading to

the formation of secondary pollutants such as smog and highly irritating gases.[4–6] Meanwhile, NO$_x$ themselves, as toxic components, can directly affect human health by decreasing lung function and causing respiratory symptoms, even at low concentrations.[7] As NO$_2$ is more active and around 30 times more toxic than NO,[8] NO$_2$ is categorized as a criteria pollutant representing NO$_x$. Thus, atmospheric NO$_2$ pollution and its control have attracted increased attention in recent decades, particularly in densely populated urban areas. For example, the concentration of roadside NO$_2$ in Hong Kong remains at a harmful level (80 μg m^{-3}),[9] which is twice the World Health Organization (WHO) standard (40 μg m^{-3}).[10] The complex and congested nature of Hong Kong makes it challenging to dilute the roadside NO$_2$. Therefore, efforts to abate atmospheric NO$_2$ should focus on both reducing NO$_2$ emissions in exhaust gases and removing NO$_2$ from the ambient air.

De-NO$_x$ technologies, such as selective catalytic reduction (SCR) and selective non-catalytic reduction (SNCR), have been extensively developed and implemented, delivering high efficiency in NO$_x$ removal (99%).[11–13] However, the operating temperature window (300–1100 °C) of these technologies makes their application prohibitive in low-temperature NO$_x$ (*e.g.*, atmospheric NO$_x$) abatement. Moreover, the generation of NH$_3$ (as a reductant) by decomposing urea solution at low temperatures (<180 °C) poses a significant challenge for the SCR

[a]School of Energy and Environment, City University of Hong Kong, Tat Chee Avenue, Kowloon, Hong Kong SAR, P. R. China. E-mail: patrick.h.sit@cityu.edu.hk; jinshang@cityu.edu.hk

[b]City University of Hong Kong Shenzhen Research Institute, Nanshan District, Shenzhen 518000, P. R. China

[c]Department of Applied Biology and Chemical Technology, The Hong Kong Polytechnic University, Hung Hom, Hong Kong SAR, P. R. China

[d]Australian Synchrotron, ANSTO, 800 Blackburn Road, Clayton, VIC 3168, Australia. E-mail: qinfeng@ansto.gov.au

[e]Institute for Superconducting & Electronic Materials, University of Wollongong, Wollongong, NSW 2522, Australia

[f]School of Energy and Environmental Engineering, University of Science and Technology Beijing, Beijing 100083, China. E-mail: ziyili@ustb.edu.cn

[g]Low-Carbon and Climate Impact Research Center, School of Energy and Environment, City University of Hong Kong, Hong Kong, P. R. China

† Electronic supplementary information (ESI) available. See DOI: https://doi.org/10.1039/d4ta04399e

‡ These authors contributed equally to this work.

This journal is © The Royal Society of Chemistry 2024

J. Mater. Chem. A, 2024, **12**, 30329–30339 | **30329**

process.[14] In addition, stricter regulations have increased the urgency for low-temperature NO_x emission control. Adsorption is considered an alternative approach for NO_x removal at low temperature. However, most adsorbents have only been evaluated for NO_x adsorption at temperatures above 80 °C,[15–17] omitting NO_2 adsorption under ambient conditions. Thus, this study aims to develop effective NO_2 adsorbents, with high NO_2 adsorption capacity and selectivity, for atmospheric NO_2 abatement at ambient temperature.

Adsorbents that exhibit a specific affinity for NO_2 with moderate strength can afford high NO_2 selectivity and capacity, making them desirable for NO_2 adsorption. Given the presence of π bonds in the NO_2 molecule, materials containing transition metal species are promising candidates for NO_2 adsorption due to their unique interaction (π-complexation) with NO_2, which enables π-backdonation from a d orbital metal center to the π* orbitals of the π-structured molecules.[18] This interaction, with moderate strength, bridges the gap between physisorption and chemisorption, enabling the π-complexation adsorbents to exhibit both high selectivity and good reversibility.[19] Copper (Cu), an affordable and abundant transition metal that has been extensively studied and used in high-temperature NO_x SCR, has emerged as a promising candidate for NO_2 adsorption.[20–24] For instance, Cu-containing carbon showed a high NO_2 removal capacity at room temperature, while the low thermal stability of carbon materials causes them to burn readily during regeneration at high temperatures.[20] Cu nanoparticle (NP) loaded silica (KCC-1) has been reported to be an effective NO_2 adsorbent, with the highly dispersed Cu NPs serving as effective adsorption sites for NO_2.[25] However, NO_2 adsorption and dissociation on Cu^{2+} and Cu^+ have not been studied. Cu-based metal–organic frameworks (MOFs) showed enhanced NO_2 adsorption due to increased porosity and the reactive adsorption of NO_2 on Cu.[24] However, the high cost and low thermal/hydrothermal stability of MOFs limit their applications in real-word gas adsorption processes.

Small-pore zeolites, characterized by their three-dimensional porous structures, high thermal stability, and large surface areas, have extensive applications in gas adsorption and separation.[26] Zeolites can also serve as unique ligands that tune the π-complexation between NO_2 and Cu.[27] Sierraalta *et al.* have demonstrated that Cu species-containing zeolites showed a stronger affinity for NO_2 molecules than those containing other transition metals (Ag and Au).[28] Onitsuka *et al.* reported that zeolites infused with Cu salts showed enhanced performance in adsorbing NO_x at a low concentration of about 5 ppm.[29] Note that extra-framework cations in zeolites are the dominant adsorption sites, whose properties dictate gas adsorption performance.[30] For instance, the valence state of these cations can affect NO_2 adsorption performance, particularly the affinity of the adsorbent for NO_2. For specific types of cations, such as Cu, their valence state is directly related to the radius and the occupancy of the valence shell. Compared with Cu^{2+}, Cu^+ and Cu^0 possess higher valence shell occupancies and fewer constraints (due to the larger radius) on the valence shell electrons, allowing more d-orbital electrons to be back-donated to the π* orbital of NO_2. Consequently, the π-complexation

occurring between NO_2 and Cu ions at lower states (Cu^+ and Cu^0) is anticipated to improve gas–host interaction, leading to a higher affinity for NO_2.

Herein, we prepared Cu^{n+}SSZ-13 zeolites ($n = 0$, 1, and 2) by reducing a Cu^{2+}-exchanged SSZ-13 zeolite under a H_2 atmosphere and systematically studied their NO_2 removal performance and mechanisms. Thanks to the formation of Cu^+ ions and the increased number of adsorption sites, Cu^{n+}SSZ-13 zeolites showed enhanced NO_2 uptake and insignificant NO release. This work suggests that the tuning of Cu species as specific binding sites in zeolites could be an effective approach for regulating the affinity of zeolites for NO_2 adsorption.

2. Experimental

2.1 Synthesis

2.1.1 Synthesis of H⁺SSZ-13 (Si/Al = 12). The synthesis of H⁺SSZ-13 (Si/Al = 12) was conducted following a previously reported method.[31] Specifically, 39.6 g of *N,N,N*-trimethyl-1-adamantanamine hydroxide (TMAdaOH, 25 wt%, Sachem Inc.) and 19.5 g of tetraethyl orthosilicate (TEOS, sigma 98%) were mixed with 4.05 g of deionized (DI) water. This mixture was stirred for 2 h at room temperature in a sealed polypropylene bottle. Afterwards, 1.05 g of aluminum ethoxide (Strem Chemical, 99%) was added to the mixture and stirred for another 1 h. The gel was then transferred into a 100 mL Teflon-lined autoclave and heated at 140 °C under static conditions for 6 days. After the crystallization, the product was filtered, thoroughly washed with DI water, and then dried at 80 °C overnight. Finally, the product was calcined in an air atmosphere at 550 °C for 8 h with a ramping rate of 2 °C min⁻¹.

2.1.2 Synthesis of Cu²⁺SSZ-13. The synthesis of Cu²⁺SSZ-13 involved a liquid-phase ion exchange process, a common approach for incorporating extra-framework cations into zeolites. Typically, 0.5 g of the as-synthesized H⁺SSZ-13 was dispersed in 50 mL of 0.5 M NH_4NO_3 and stirred for 12 h at 80 °C, with the process being repeated four times to ensure thorough ion exchange. The resulting NH_4^+SSZ-13 product was filtered, thoroughly washed with DI water, and dried at 80 °C overnight. Then, 0.5 g of the as-synthesized NH_4^+SSZ-13 was dispersed in 50 mL of 0.5 M $Cu(NO_3)_2$ solution and stirred for 12 h at 80 °C, again being repeated four times. The resulting Cu²⁺SSZ-13 was collected by filtration, washed extensively with DI water, and dried at 353 K overnight.

2.1.3 Synthesis of H₂-reduced Cu^{n+}SSZ-13 samples. A series of Cu^{n+}SSZ-13 samples were prepared by reducing Cu²⁺SSZ-13 under a H_2 atmosphere at various temperatures. H_2-temperature programmed reduction (TPR) was conducted on a Micromeritics ASAP 2950 instrument to identify optimal reduction conditions for the preparation of Cu^{n+}SSZ-13. The signal of H_2 during the reduction process was detected using a thermal conductivity detector (TCD). Then, 0.1 g of Cu²⁺SSZ-13 was placed in a tube furnace and thermally treated under argon at 350 °C (ramping rate = 2 °C min⁻¹) for 4 h to remove the pre-adsorbed impurities. After cooling to room temperature, 5% H_2 (balanced with Ar, 20 cc min⁻¹) was continuously purged and Cu²⁺SSZ-13 was heated at 100 °C to 700 °C for 3 h (ramping

30330 | *J. Mater. Chem. A*, 2024, **12**, 30329–30339

This journal is © The Royal Society of Chemistry 2024

rate = 2 °C min^{-1}). The resulting products are named Cu^{n+}SSZ-13-reducing temperature-R (*e.g.*, Cu^{n+}SSZ-13-100-R).

2.2 Characterization

Synchrotron powder X-ray diffraction (PXRD) was measured using a Mythen-II detector at the PD beamline, Australian Synchrotron, ANSTO. To understand the valence state and the coordination environment of the Cu ions in Cu^{n+}SSZ-13 samples, Cu K-edge X-ray absorption near-edge structure (XANES) and extended X-ray absorption fine structure (EXAFS) spectra were collected at the XAS beamline, Australian Synchrotron, ANSTO. The morphologies of the samples were investigated using a scanning electron microscope (SEM) (EVO MA10, ZEISS, Germany). The specific surface area and pore volume of Cu^{n+}SSZ-13-190-R before and after NO$_2$ dynamic column adsorption, as well as fresh H$^+$SSZ-13, were determined using a 3Flex Surface Characterization Analyzer (Micromeritics Instrument Corp., USA) using N$_2$ at −196 °C. Prior to measurement, the samples were degassed on the 3Flex Surface Characterization Analyzer at 300 °C for 3 h. The chemical composition (*e.g.*, Si/Al and metal/Al ratios) of the samples was determined by Energy dispersive spectroscopy (EDX) using an EDX detector (Oxford Aztec Energy X-MAX 50) installed in a SEM (FEI Quanta 450 FEG). The *in situ* Fourier Transform Infrared (FTIR) spectra of Cu^{n+}SSZ-13-190-R were recorded on an IRAffinity-1 FTIR spectrophotometer (Shimadzu, Japan) at 25 °C, with an NO$_2$ concentration of 1000 ppm and a flow rate of 60 mL min^{-1}. Before the measurement, Cu^{n+}SSZ-13-190-R was thermally treated in the FTIR cell under a N$_2$ atmosphere at 200 °C for 8 h to remove the pre-adsorbed gases and moisture.

2.3 Fixed-bed NO$_2$/NO dynamic column adsorption at room temperature

The dynamic column breakthrough (DCB) of NO$_x$ was measured using a fixed-bed system (Fig. S1†) under ambient conditions (25 °C, 1 bar). The adsorbent (0.1 g) was well mixed with non-reactive glass beads (3 mm in diameter) to generate a homogeneous bed, and then packed into a stainless-steel tube. Unless otherwise specified, the samples were degassed at 300 °C under argon before NO$_x$ adsorption until the pre-adsorbed moisture was completely removed, as monitored by a Mass Spectrometer (Stanford Research Systems UGA300). Subsequently, NO$_2$ or NO (both at 1000 ppm) in helium was purged through the column at a total inlet flow rate of 60 mL min^{-1} at 25 °C. The concentrations of NO$_2$ and NO in the outlet gas were measured using an electrochemical sensor (RAE Systems, MultiRAE Plus PGM-50/5P).

2.4 Density functional theory (DFT) calculation

DFT calculations were performed using the QUANTUM ESPRESSO package.[32–35] Ultrasoft pseudopotentials with the Perdew–Burke–Ernzerhof exchange–correlation functional were employed.[36] The plane wave cutoffs were 30 Ry and 240 Ry for wavefunctions and the augmented charge density, respectively. The semiempirical Grimme's DFT-D3 scheme was used for van der Waals interaction correction.[37] The SSZ-13 zeolite has a 1 ×

1 × 1 supercell with a total trigonal P supercell size of 13.675 Å × 13.675 Å × 14.767 Å. Three Si atoms were replaced with Al atoms. To maintain the charge balance, hydrogen atoms were added near the Al atoms according to the charge of the inserted transition metal ions. The 6-membered ring (6MR) has been identified as the most favorable location for the extra-framework cations.[38] Thus, we examined the local structures of the Cu ions in the 6MR, with 2 Si atoms being replaced by 2 Al atoms.

3. Results and discussion

3.1 Characterization of adsorbents

Cu^{2+}SSZ-13 was prepared from H$^+$SSZ-13 by an ion-exchange method, where Cu^{2+} substituted the extra-framework H$^+$ cations (Fig. 1a). The synchrotron PXRD patterns of Cu^{2+}SSZ-13 indicated the high purity and crystallinity characteristic of chabazite (CHA)-type SSZ-13 zeolite (Fig. 1b). As displayed in the SEM image (Fig. 1c), Cu^{2+}SSZ-13 particles possess an elliptical shape and smooth exterior surfaces. Cu^{n+}SSZ-13 zeolites were then prepared by reducing Cu^{2+}SSZ-13 under H$_2$. Prior to the reduction, H$_2$-TPR was conducted to determine the optimal reduction temperature (Fig. 1d). With the temperature increasing, two H$_2$ consumption peaks appeared at around 200 and 400 °C, which were attributed to the reduction of Cu^{2+} at various locations within the zeolite.[39] It is noteworthy that Cu^{2+} ions at different locations within the zeolite require different energy levels to be reduced. For example, the six-membered ring (6MR) in CHA is the most stable site for Cu^{2+}, demanding more energy for reduction than those situated at an eight-membered ring (8MR).[40,41] To achieve varying levels of Cu^{2+} reduction in SSZ-13 zeolite, both low (≤250 °C) and high temperature (≥390 °C) ranges were adopted.

Upon high-temperature reduction (390, 490, and 750 °C), the structure of Cu^{n+}SSZ-13 samples remained intact, as evidenced by the unchanged PXRD peak locations of Cu^{n+}SSZ-13 and Cu^{2+}SSZ-13 (Fig. 2a). However, the undesirable formation of Cu^0 occurred on the external surface of the zeolite (Fig. 2c). Rietveld refinement of PXRD indicated that the crystallite size of these Cu^0 particles (17, 23, and 25 nm at 390, 490, and 750 °C, respectively) increased with the increasing reduction temperature (Fig. S2†). The X-ray absorption spectroscopy (XAS) results showed that higher reduction temperatures resulted in a shift towards lower energy and a reduction in intensity of the white line peak (Fig. 2b), corresponding to decreases in the valence state and the occupancy of d orbitals of Cu ions.[42] These observations suggest that during the reduction, Cu^{2+} migrated from the supercage to the external surface of zeolites and aggregated to form metallic Cu particles (Fig. 2c). This mitigation process can be explained by the *R*-plot EXAFS spectra (Fig. 2b, inset). Two peaks appearing at 1.7 Å and 2.2 Å were ascribed to the Cu–O and Cu–Cu bonds, respectively, arising from the coordination of Cu ions with lattice oxygen atoms in the zeolite (Cu–O) and Cu–Cu bonds in elementary Cu.[43] The intensity of the Cu–O peak decreased while that of the Cu–Cu peak increased upon reduction at higher temperatures, indicating that more Cu^{2+} migrated from the cage to the external

This journal is © The Royal Society of Chemistry 2024

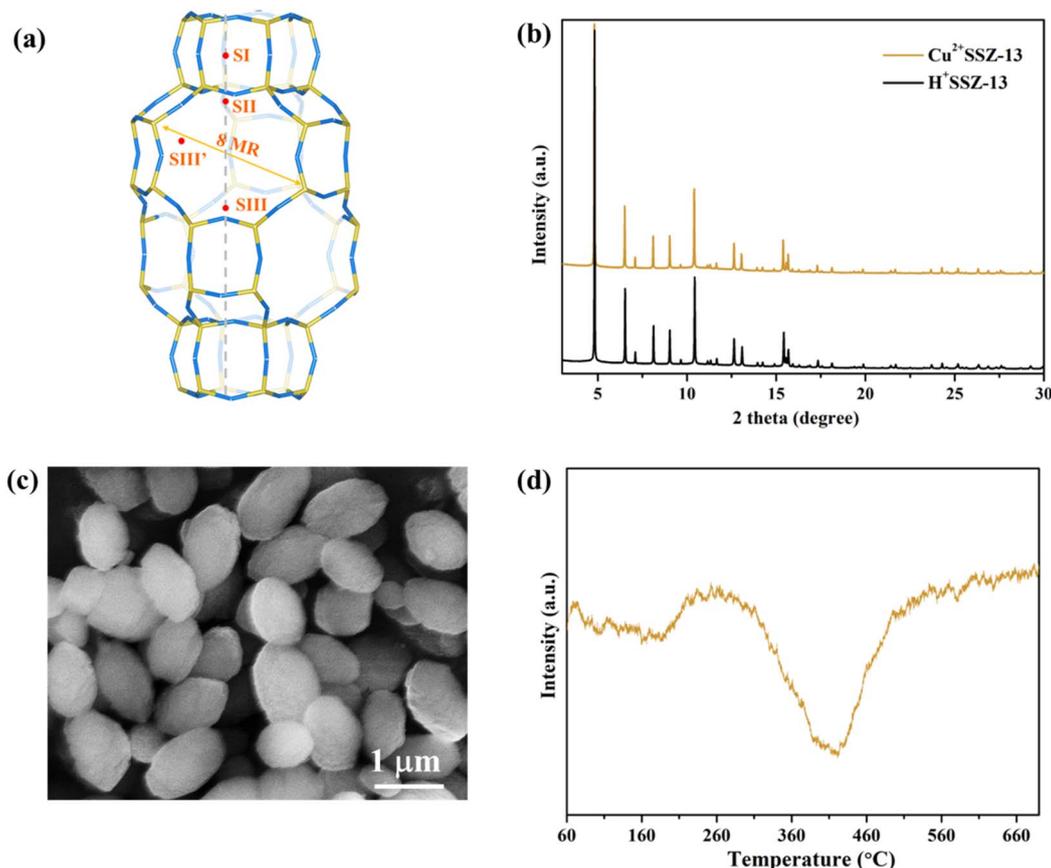*J. Mater. Chem. A*, 2024, **12**, 30329–30339 | **30331**

Fig. 1 (a) Illustration of the local crystal structure of chabazite (CHA) zeolites. SI–SIII′ are the possible positions of extra-framework cations; (b) synchrotron powder X-ray diffraction patterns of Cu^{2+}SSZ-13 and pristine H^{+}SSZ-13 (wavelength = 0.7735 Å); (c) SEM image of Cu^{2+}SSZ-13; and (d) H_2-TPR profile of Cu^{2+}SSZ-13.

surface of zeolites to form elementary Cu. This result is consistent with the reduced lattice parameters of Cu^{n+}SSZ-13 at high reduction temperatures (Fig. 2d), which was attributed to the contraction of the zeolite lattice due to negative thermal expansion.[44]

It is acknowledged that the well dispersed extra-framework cations in zeolites serve as the dominant active adsorption sites for gas molecules.[27,45,46] Therefore, the presence of bulk Cu^{0} NPs on the external surface of zeolites should be minimized. Consequently, a further decrease in the reduction temperature was implemented. No characteristic peaks of elementary Cu were observed in the PXRD patterns of Cu^{n+}SSZ-13 samples reduced at 100, 150, 170 and 190 °C (Fig. 3a), indicating the absence of Cu^{0}. The XAS results showed the changes in Cu^{2+}/Cu^{+} levels within zeolites (Fig. 3b). The weak absorption peak ranging between 8975 and 8980 eV is the fingerprint of Cu^{2+}, which is assigned to a dipole-forbidden 1s → 3d transition.[47] The characteristic peak of Cu^{+} was observed at 8980–8985 eV, corresponding to the 1s → 4p transition.[48] As the reduction temperature increased, the Cu^{2+} peak at 8978 eV diminished, while the Cu^{+} peak at 8984 eV gradually increased, suggesting that a higher reduction temperature facilitated the conversion of Cu^{2+} to Cu^{+}. The edge peak at 8993–8997 eV, known as the 'white line' of Cu^{2+}, indicates a higher oxidation

state when the peak intensity is greater.[48] As the reduction temperature increased, the intensity of the white line decreased, further suggesting a transformation of Cu^{2+} to Cu^{+}.

3.2 NO₂ adsorption

The NO_2 adsorption performance of Cu^{n+}SSZ-13 reduced at different temperatures (*i.e.*, 100, 150, 170, and 190 °C) was validated by NO_2 dynamic adsorption at room temperature (Fig. 4a). Prior to NO_2 adsorption, the adsorbents were activated at 300 °C under Ar to remove the pre-adsorbed impurities. The NO_2 adsorption capacity of the Cu^{n+}SSZ-13 samples increased with the increasing reduction temperature (Fig. 4b), which is attributed to a higher proportion of Cu^{+} being present at a higher reduction temperature. The linear correlation between the NO_2 capacity and the reduction temperature encouraged us to tentatively raise the reduction temperature to 250 °C, intending to further improve the NO_2 adsorption capacity. However, the NO_2 adsorption over Cu^{n+}SSZ-13-250-R was found to be even lower than that of the unreduced sample (Cu^{2+}SSZ-13). This result was caused by the formation of Cu^{0} particles on the external surface of the zeolite (see the SEM image in Fig. S3†), which reduced the number of accessible active adsorption sites for NO_2 molecules. The highest NO_2 adsorption
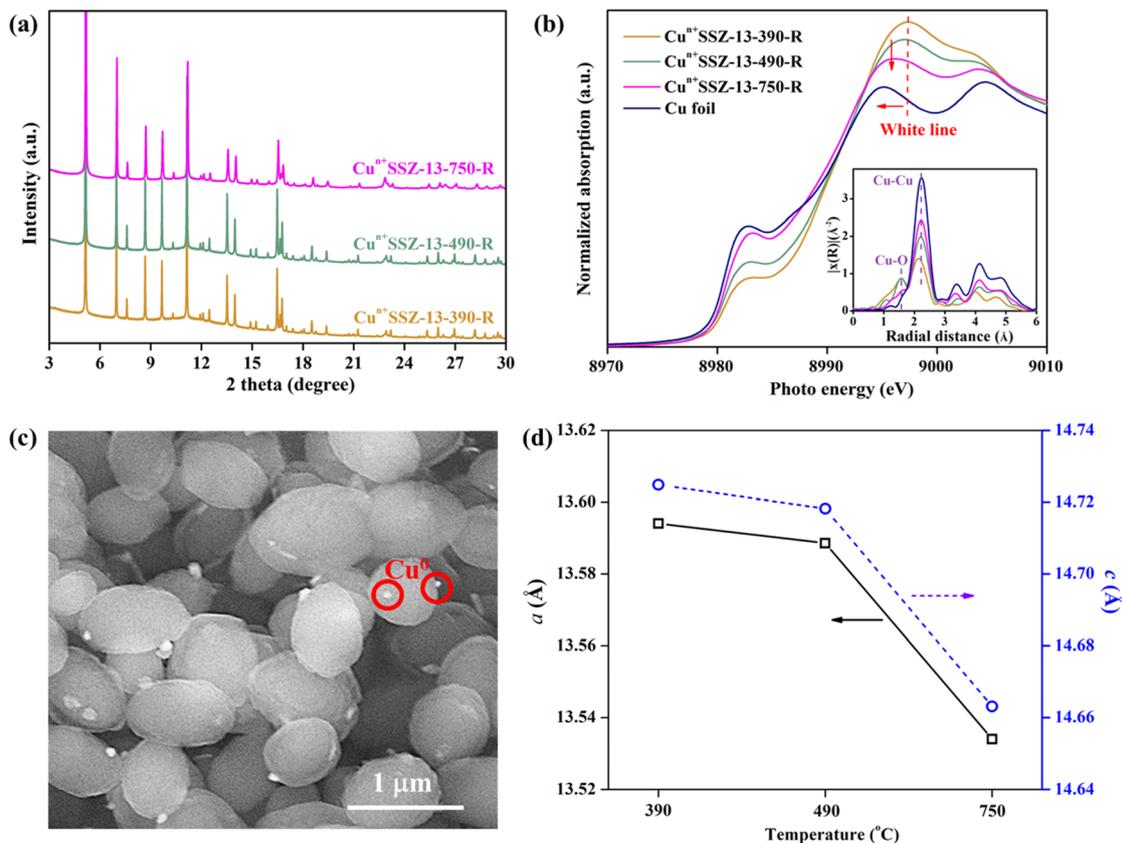
30332 | *J. Mater. Chem. A*, 2024, **12**, 30329–30339

This journal is © The Royal Society of Chemistry 2024

Fig. 2 (a) PXRD patterns (wavelength: 0.8275 Å) and (b) Cu K-edge XAS spectra of $Cu^{n+}SSZ$-13 reduced by H_2 at 390, 490, and 750 °C (inset: Fourier transformed EXAFS modulation with phase correction in the k-range of 3.0–12.5 Å^{-1}, k^2-weighted); (c) SEM image of $Cu^{n+}SSZ$-13-390-R; and (d) variation of unit cell parameters (a and c) of $Cu^{n+}SSZ$-13 in relation to the H_2-reduction temperature.

capacity, achieved by $Cu^{n+}SSZ$-13-190-R, was 1.79 mmol g^{-1} (Fig. 4b). This capacity demonstrated a significant increase of 19.4% and 52.3% with respect to that of $Cu^{2+}SSZ$-13 and pristine H^+SSZ-13, respectively, substantially surpassing the performance of the reported metal-modified zeolites (Table S1†). The above results clearly show that the H_2 reduction of $Cu^{2+}SSZ$-13 effectively improves the NO_2 adsorption capacity, which is attributed to the increased affinity of binding sites for NO_2.

To assess the impact of NO_2 adsorption on the specific surface area and pore volume of the Cu-modified zeolite, N_2 adsorption–desorption isotherms were recorded for $Cu^{n+}SSZ$-13-190-R before and after NO_2 dynamic adsorption (Fig. 4c, d and Table S2†). Post-adsorption, the BET surface area of $Cu^{n+}SSZ$-13-190-R remained largely unchanged, while the pore volume slightly increased from 0.34 to 0.40 cm^3 g^{-1} which was probably due to the formation of additional interparticle
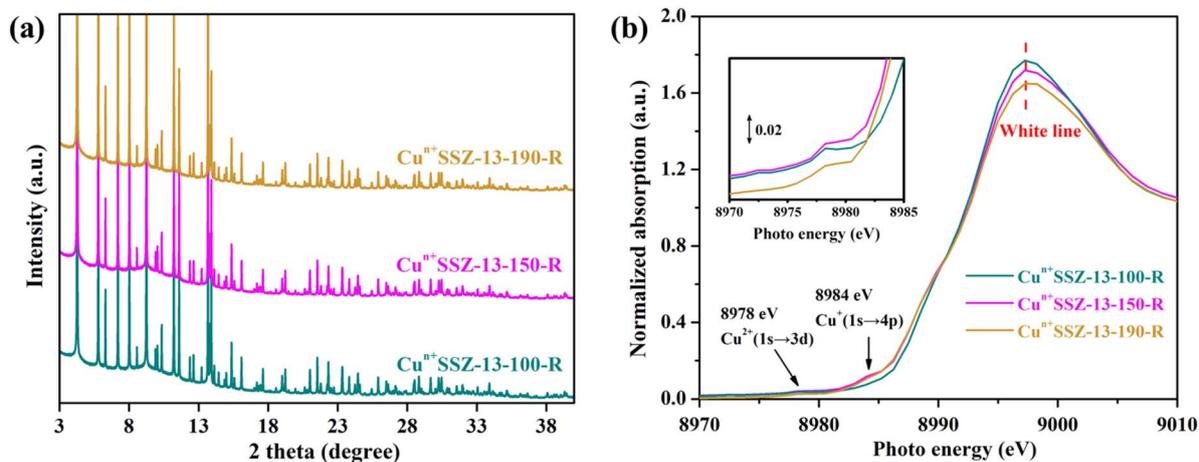

Fig. 3 (a) PXRD patterns (wavelength of 0.6880 Å) and (b) Cu K-edge XAS of $Cu^{n+}SSZ$-13 reduced by H_2 at 100, 150, 170 and 190 °C.
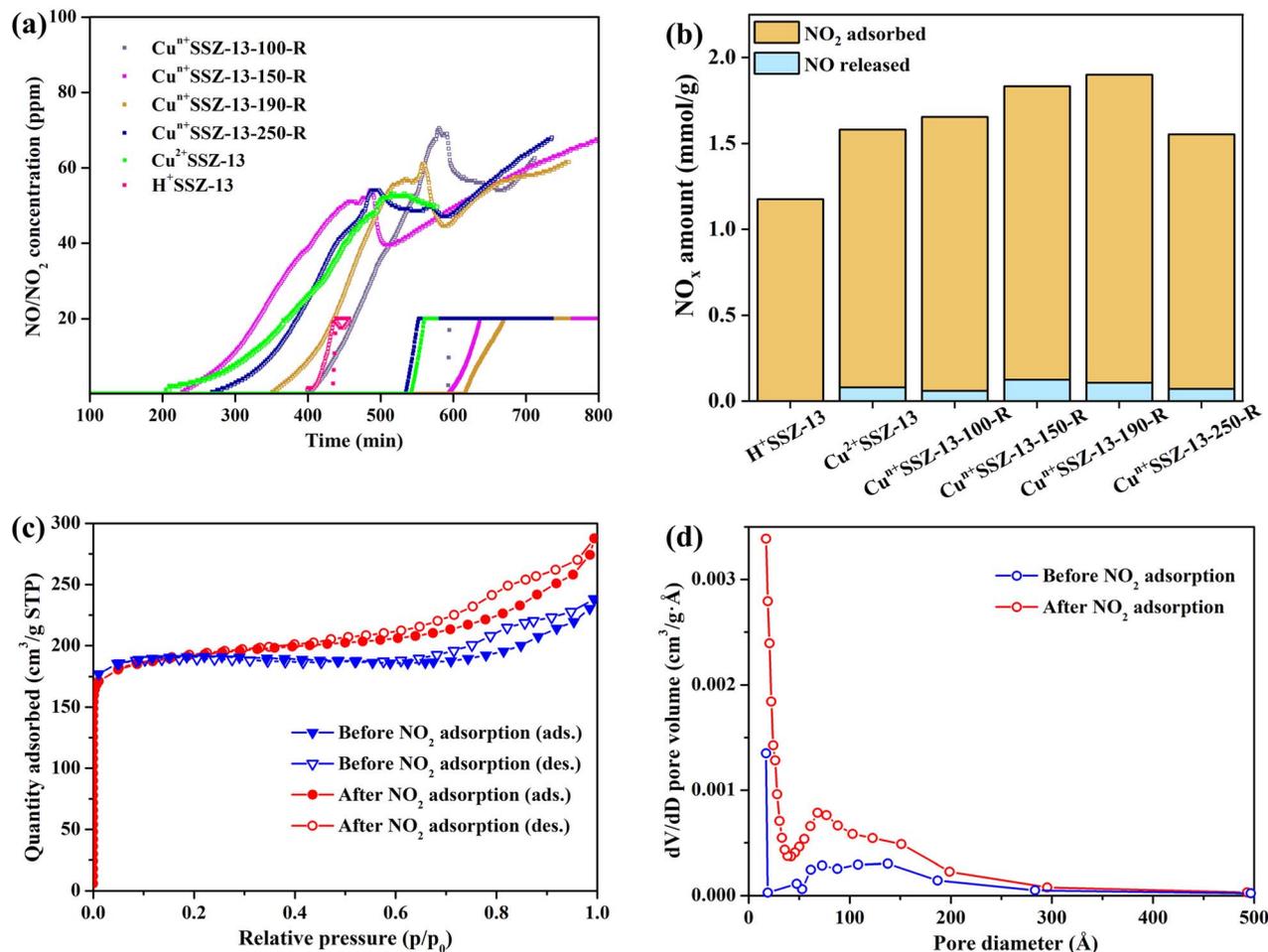
This journal is © The Royal Society of Chemistry 2024

J. Mater. Chem. A, 2024, **12**, 30329–30339 | **30333**

Fig. 4 (a) NO_2 (1000 ppm) dynamic column adsorption at room temperature on H^+SSZ-13, Cu^{2+}SSZ-13 and Cu^{n+}SSZ-13 samples with thermal activation. The hollow (□) and solid (■) dots represent the concentration of NO and NO_2, respectively. (b) The corresponding NO_2 adsorption capacity and NO released amount. (c) N_2 adsorption–desorption isotherms (−196 °C) and (d) pore size distributions of Cu^{n+}SSZ-13-190-R before and after NO_2 (1000 ppm) dynamic column adsorption.

stacking pores. Therefore, the porous structures of Cu^{n+}SSZ-13-190-R remained largely unaffected after a cycle of NO_2 dynamic adsorption. It is anticipated that the lifespan and adsorption capacity of Cu^{n+}SSZ-13-190-R can be substantially preserved by regenerating it through a gentle heating process to drive off adsorbed water and NO_2. Furthermore, in comparison with H^+SSZ-13 without Cu modification, which featured micropores with a Brunauer–Emmett–Teller (BET) surface area of 771.69 m^2 g^{-1} and a pore volume of 0.38 cm^3 g^{-1} (Fig. S4†), Cu^{n+}SSZ-13-190-R exhibited a micro-mesoporous structure with a reduced surface area (557.97 m^2 g^{-1}) and pore volume (0.34 cm^3 g^{-1}). Despite the larger surface area and pore volume of the unmodified H^+SSZ-13, the Cu-modified Cu^{n+}SSZ-13-190-R demonstrated a higher NO_2 adsorption capacity. This finding suggests that the incorporation of Cu into the SSZ-13 zeolite significantly enhances the NO_2 adsorption process, playing a more important role than the surface area and pore volume. Therefore, while surface area and pore volume are important factors in adsorption processes, the unique role of Cu within the SSZ-13 zeolite is the key determinant for the improved NO_2 removal performance.

To evaluate the effect of moisture on NO_2 adsorption, experiments were conducted on non-activated Cu^{n+}SSZ-13 samples (*i.e.*, without thermal treatment prior to NO_2 adsorption). Compared with Cu^{2+}SSZ-13, the non-activated Cu^{n+}SSZ-13 samples showed a decreased NO_2 capacity and an increased release of NO (Fig. S5†). The decline in capacity was due to the presence of moisture within zeolites generated during the H_2 reduction process (eqn (1)). Such moisture would poison the active adsorption sites (Cu ions) by forming Cu hydrates and blocking sites intended for NO_2 adsorption, thereby reducing the NO_2 capacity. FTIR analysis (Fig. S6†) suggested that the moisture could facilitate NO_2 transformation into NO_3^- and gaseous NO (eqn (2)).[49] After a certain time, the amount of released NO decreased, and the NO release curves stabilized, suggesting the moisture was gradually consumed by NO_2. Therefore, the thermal activation process is essential to mitigate the negative effects of moisture on NO_2 adsorption.

$$2Cu(OH)^+ + H_2 \rightarrow 2Cu^+ + 2H_2O \qquad (1)$$

$$3NO_2 + H_2O \rightarrow 2HNO_3 + NO(g) \qquad (2)$$
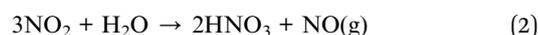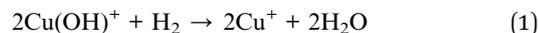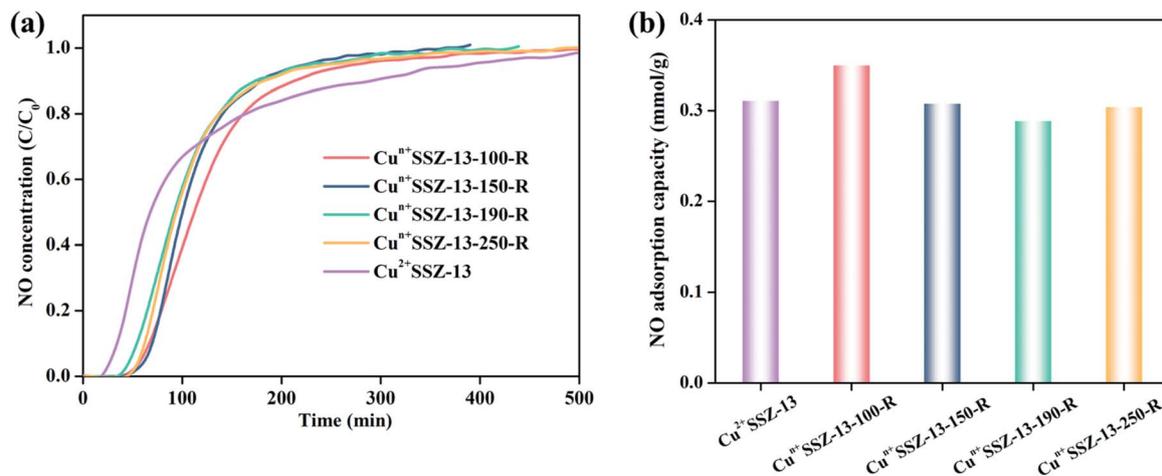
Fig. 5 (a) NO (1000 ppm) dynamic adsorption on Cu^{n+}SSZ-13 samples at room temperature; and (b) the corresponding NO adsorption capacity.

In addition to improving NO_2 capacity, moisture removal also contributed to the decrease of NO release, which was evident from the longer NO retention time and the more gradual slopes of NO release curves (Fig. 4a). However, the correlation between the amount of NO released and the reduction temperature was inconsistent, which resulted from the different NO retention abilities of the samples. For example, Cu^{n+}SSZ-13-100-R showed the highest NO adsorption capacity (Fig. 5), aligning with the lowest amount of NO released (Fig. 4b). The NO adsorption capacity decreased with the increasing reduction temperature from 100 to 190 °C, while it

increased when the reduction temperature was further raised to 250 °C.

Our Cu^{n+}SSZ-13 adsorbent, which exhibits an enhanced capacity for ambient NO_2 abatement yet sensitivity to moisture, can be effectively used for the reduction of NO_2 emission from the engine pipeline when combined with desiccant materials or condensation systems that remove moisture from the exhaust gas. Additionally, our zeolite can be used in air purifiers or industrial settings to remove NO_2, incorporating moisture control mechanisms such as heating elements or moisture-absorbing materials. Given the well-preserved specific surface area and pore volume after NO_2 adsorption, as evidenced by
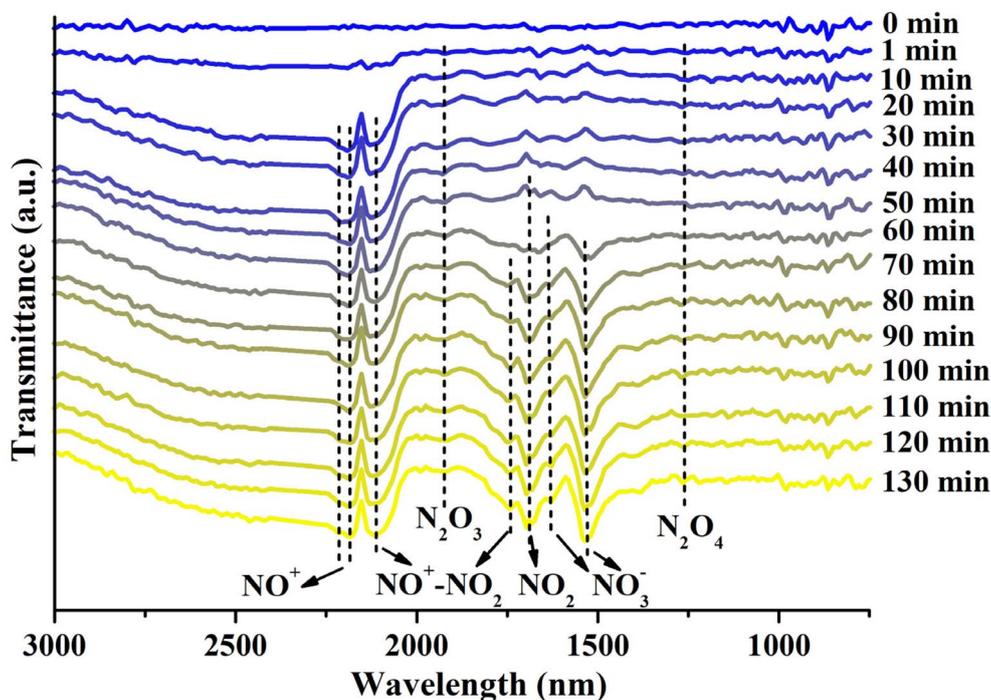
Fig. 6 *In situ* FTIR spectra of Cu^{n+}SSZ-13-190-R during NO_2 adsorption, with the background of the fresh sample subtracted (conditions: NO_2 concentration of 1000 ppm, flow rate of 60 mL min^{-1}, 25 °C).

This journal is © The Royal Society of Chemistry 2024

J. Mater. Chem. A, 2024, **12**, 30329–30339 | **30335**

porous property analysis, the Cu^{n+}SSZ-13-190-R adsorbent is expected to maintain its performance over multiple cycles of adsorption and thermal regeneration, thereby ensuring a long lifespan in the aforementioned practical applications.

3.3 Discussion of the mechanism

To elucidate the mechanism of NO_2 adsorption on our Cu-modified zeolite, *in situ* FTIR analysis of the Cu^{n+}SSZ-13-190-R zeolite during the NO_2 adsorption process was carried out (Fig. 6). The FTIR spectra revealed the presence of adsorbed NO_2 at 1690 cm^{-1},[50] which tended to form an N_2O_4 dimer (1261 cm^{-1})[51] in small-pore zeolites due to the confinement effect.[45] The adsorbed N_2O_4 can undergo ionization in the zeolite to form NO_3^- an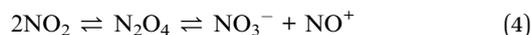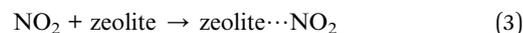d NO^+.[52,53] As anticipated, the formation of nitrites was observed, including bridging NO_3^- (1630 cm^{-1}) and monodentate NO_3^- (1534 cm^{-1}).[54,55] Meanwhile, the asymmetric band at around 2178 cm^{-1}, corresponding to two NO^+ stretches at 2214 and 2178 cm^{-1}, is indicative of the generation of NO^+ intermediates,[56] which can serve as an adsorption site for NO_2.[45] The formation of NO^+–NO_2 complexes was confirmed by the presence of an N–O stretch at 1741 cm^{-1} accompanied by another NO stretch at 2109 cm^{-1},[56] as well as a weak band at 1925 cm^{-1} assigned to N_2O_3,[54] a product of NO_2

adsorption on NO^+.[57] Although a small amount of NO was released during NO_2 adsorption due to NO_2 dissociation caused by oxygen vacancies, no distinct FTIR peaks indicative of adsorbed NO were observed. Based on these findings, the mechanism for NO_2 adsorption on the Cu^{n+}SSZ-13-190-R zeolite during adsorption was proposed, as shown in eqn (3)–(6).

$$NO_2 + zeolite \rightarrow zeolite \cdots NO_2 \quad (3)$$

$$2NO_2 \rightleftharpoons N_2O_4 \rightleftharpoons NO_3^- + NO^+ \quad (4)$$

$$2NO^+ + 2NO_2 \rightarrow NO^+ \cdots NO_2 + N_2O_3 \quad (5)$$

$$NO_2 + O_{vac} \rightarrow O_{vac} \cdots O + NO \text{ (small amount)} \quad (6)$$

To understand the effects of copper valence states on NO_2 adsorption in zeolites, DFT calculations were conducted to study the electronic and structural changes associated with Cu^+ and Cu^{2+} ions upon NO_2 adsorption. As shown in Fig. S7,† the number of cations (Cu^+ and H^+) in the zeolite after H_2 reduction is increased. As the cations would serve as major adsorption sites, the increase in cation density would afford more binding sites for NO_2 adsorption. Moreover, as shown in Table 1, the formation of Cu^+ (binding energy of 20.06 kcal mol^{-1}), which has a higher affinity for NO_2 than Cu^{2+} (binding energy of 14.36 kcal mol^{-1}), strengthens the interaction with NO_2 through π-complexation. Thus, the increase in the density of adsorption sites with increasing binding strength enables greater NO_2 uptake.

The optimized local structures of NO_2/NO adsorbed on Cu^+ and Cu^{2+} in SSZ-13 zeolites were analyzed (Fig. 7). When NO_2 or NO is adsorbed, Cu–O bonds are partially disrupted, and the

Table 1 The binding energy (kcal mol^{-1}) of NO_2 and NO molecules upon adsorption on Cu^+ and Cu^{2+} in the SSZ-13 zeolite calculated by density functional theory (DFT)

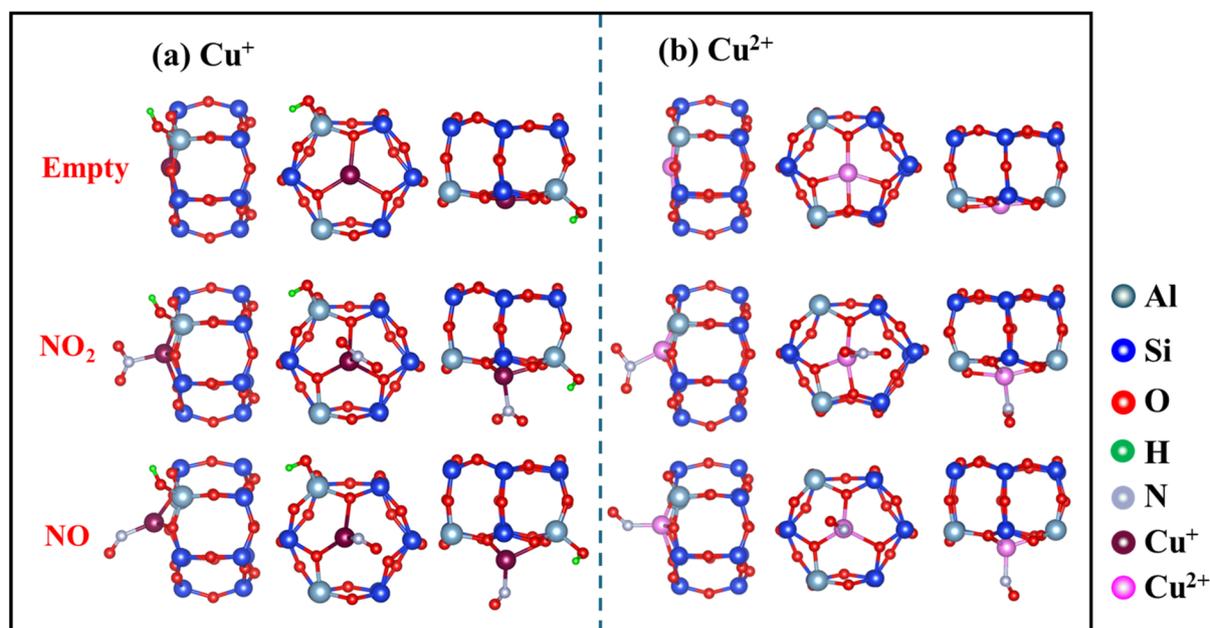|	NO_2	NO
Cu^+	−20.06	−30.31
Cu^{2+}	−14.36	−30.78

Fig. 7 Comparison of optimized local structures of NO_2/NO adsorbed on Cu^+ and Cu^{2+} cations in the SSZ-13 zeolite. The top, middle, and bottom images respectively depict the naked cation, and the cation interacting with NO_2 and NO, all located at the 6 MR sites.

30336 | *J. Mater. Chem. A*, 2024, **12**, 30329–30339

This journal is © The Royal Society of Chemistry 2024

Table 2 Changes in electron occupancies (ΔOc) in the outer-shell orbitals of N, O and transition metal ions upon NO$_2$ adsorption (Lowdin). Data was derived from the electron occupancies before and after NO$_2$ and NO adsorption on Cu$^+$SSZ-13 and Cu^{2+}SSZ-13 zeolites (Table S3)

	N-2s	N-2p$_z$	N-2p$_x$	N-2p$_y$	O-2s	O-2p$_z$	O-2p$_x$	O-2p$_y$	O-2s	O-2p$_z$	O-2p$_x$	O-2p$_y$	Cu-3d$_{z^2}$	Cu-3d$_{zx}$	Cu-3d$_{zy}$	Cu-3d$_{x^2-y^2}$	Cu-3d$_{xy}$	Cu-4s	Cu-4p$_z$	Cu-4p$_x$	Cu-4p$_y$	$\sum$3d	$\sum$4s + 4p
Cu$^+$ + NO$_2$	−0.09	0.32	−0.08	−0.16	−0.01	0.23	−0.12	−0.12	−0.02	0.18	−0.08	−0.12	−0.37	−0.05	−0.07	0.16	0.00	−0.01	0.16	0.01	0.01	−0.32	0.17
Cu$^+$ + NO	−0.28	0.11	0.05	0.06	−0.01	0.10	−0.03	−0.05	0.00	0.00	0.00	0.00	−0.02	−0.18	−0.16	0.15	−0.06	0.05	0.16	−0.04	−0.01	−0.27	0.16
Cu^{2+} + NO$_2$	−0.10	0.31	−0.09	−0.15	−0.01	0.21	−0.13	−0.10	−0.02	0.19	−0.09	−0.13	−0.34	−0.09	−0.06	0.46	0.00	0.01	0.14	0.02	−0.01	−0.03	0.15
Cu^{2+} + NO	−0.23	−0.04	−0.03	0.06	−0.02	0.01	−0.07	−0.06	0.00	0.00	0.00	0.00	−0.17	−0.19	−0.17	0.47	−0.03	0.01	0.19	0.00	−0.01	−0.08	0.19

position of Cu ions shifts from a planar arrangement to a non-planar one. These changes in Cu–O coordination numbers and the displacement of Cu ion positions can indicate the intensity of interaction with NO$_x$. Calculations showed reduced electron occupancies (ΔOc) in the 3d orbitals and increased ΔOc in the 4s and 4p orbitals (Table 2), suggesting σ-donation from NO$_2$ and π-backdonation from Cu ions, respectively. In addition, Cu^{2+} (0.72 Å) has a smaller radius than Cu$^+$ (0.96 Å) and attracts electrons more tightly.[26] This constraint resulted in more stable electrons in the d orbitals of Cu^{2+}, making it more difficult to enable backdonation to the π* orbital of NO$_2$ and thus weakening the interaction with NO$_2$. Thus, the higher affinity of Cu$^+$ for NO$_2$ than Cu^{2+}, which is attributed to the more efficient π-complexation, facilitates NO$_2$ adsorption by Cu^{n+}SSZ-13.

4. Conclusions

In this work, in-depth analysis of NO$_2$ adsorption on Cu^{n+}SSZ-13 zeolites under ambient conditions was conducted, including evaluation of NO$_2$ uptake, NO release, the affinity of adsorption sites for NO$_2$, and the underlying adsorption mechanisms. Among the Cu-modified zeolites investigated, Cu^{n+}SSZ-13-190-R exhibited the highest NO$_2$ adsorption capacity, outperforming both H$^+$SSZ-13 and Cu^{2+}SSZ-13. Our experimental and DFT studies demonstrated that the enhanced NO$_2$ adsorption was attributed to the formation of abundant Cu$^+$ ions within the zeolite, which have a higher affinity for NO$_2$ than Cu^{2+}, as well as the increased amount of adsorption sites. The elimination of moisture and Cu^0 formed upon Cu^{2+}SSZ-13 reduction was favorable for NO$_2$ adsorption. The findings of this research could provide valuable insights for the development of adsorbents for NO$_2$ removal at ambient temperature.

Data availability

The datasets generated and/or analyzed during the current study are available from the corresponding author upon reasonable request.

Conflicts of interest

There are no conflicts to declare.

Acknowledgements

This journal is © The Royal Society of Chemistry 2024

J. Mater. Chem. A, 2024, **12**, 30329–30339 | **30337**

References

1 Z. Chen, J.-N. Wang, G.-X. Ma and Y.-S. Zhang, *Lancet*, 2013, **382**, 1959.

2 V. L. Feigin, G. A. Roth, M. Naghavi, P. Parmar, R. Krishnamurthi, S. Chugh, G. A. Mensah, B. Norrving, I. Shiue and M. Ng, *Lancet Neurol.*, 2016, **15**, 913–924.

3 P. M. Edwards, S. S. Brown, J. M. Roberts, R. Ahmadov, R. M. Banta, J. A. Degouw, W. P. Dube, R. A. Field, J. H. Flynn and J. B. Gilman, *Nature*, 2014, **514**, 351–354.

4 P. Georgopoulos, S. Arunachalam and S. Wang, *J. Air Waste Manage. Assoc.*, 1997, **47**, 838–850.

5 D. Pudasainee, B. Sapkota, M. L. Shrestha, A. Kaga, A. Kondo and Y. Inoue, *Atmos. Environ.*, 2006, **40**, 8081–8087.

6 M. Shao, Y. Zhang, L. Zeng, X. Tang, J. Zhang, L. Zhong and B. Wang, *J. Environ. Manage.*, 2009, **90**, 512–518.

7 G. B. Marks, W. Ezz, N. Aust, B. G. Toelle, W. Xuan, E. Belousova, C. Cosgrove, B. Jalaludin and W. T. Smith, *Environ. Health Perspect.*, 2010, **118**, 1476–1482.

8 R. Pastel and R. Sausa, *Appl. Opt.*, 1996, **35**, 4046–4052.

9 The Government of the Hong Kong Special Administrative Region - Press Releases, *EPD announces air quality monitoring results in 2019*, 2020, https://www.info.gov.hk/gia/general/202001/20/P2020012000874.htm.

10 Z. Hu, Z. Shen and J. C. Yu, *Environ. Sci. Technol.*, 2017, **51**, 7076–7083.

11 J. W. Girard, C. Montreuil, J. Kim, G. Cavataio and C. Lambert, *SAE Int. J. Fuels Lubr.*, 2009, **1**, 488–494.

12 C. Lambert, R. Hammerle, R. McGill, M. Khair and C. Sharp, *SAE Trans.*, 2004, 580–589.

13 L. Muzio, G. Quartucy and J. Cichanowiczy, *Int. J. Environ. Pollut.*, 2002, **17**, 4–30.

14 V. Schmeisser, M. Weibel, L. S. Hernando, I. Nova, E. Tronconi and M. P. Ruggeri, *SAE Int. J. Commer. Veh.*, 2013, **6**, 190–199.

15 H.-Y. Chen, J. E. Collier, D. Liu, L. Mantarosie, D. Durán-Martín, V. Novák, R. R. Rajaram and D. Thompsett, *Catal. Lett.*, 2016, **146**, 1706–1711.

16 C. Wan and J. Li, *Carbohydr. Polym.*, 2015, **134**, 144–150.

17 Y. Zheng, L. Kovarik, M. H. Engelhard, Y. Wang, Y. Wang, F. Gao and J. n. Szanyi, *J. Phys. Chem. C*, 2017, **121**, 15793–15803.

18 R. T. Yang, *Adsorbents: Fundamentals and Applications*, John Wiley & Sons, 2003.

19 A. Takahashi, R. T. Yang, C. L. Munson and D. Chinn, *Langmuir*, 2001, **17**, 8405–8413.

20 M. Sun, A. Hanif, T. Wang, Q. Gu and J. Shang, *Sep. Purif. Technol.*, 2023, **314**, 123563.

21 Y. Tian, M. Kong, Z. Tao, C. Yang, S. Shang, Q. Gu, D. C. Tsang, L. Li and J. Shang, *J. Hazard. Mater.*, 2023, **441**, 129962.

22 M. Sun, A. Hanif, T. Wang, C. Yang, D. C. Tsang and J. Shang, *J. Hazard. Mater.*, 2021, **418**, 126400.

23 S. Shang, C. Yang, Y. Tian, Z. Tao, A. Hanif, M. Sun, H. H. S. Wong, C. Wang and J. Shang, *ACS ES&T Eng.*, 2020, **1**, 375–384.

24 S. Shang, C. Yang, C. Wang, J. Qin, Y. Li, Q. Gu and J. Shang, *Angew. Chem., Int. Ed.*, 2020, **59**, 19680–19683.

25 B. Levasseur, A. M. Ebrahim and T. J. Bandosz, *J. Colloid Interface Sci.*, 2012, **377**, 347–354.

26 M. Sun, Q. Gu, A. Hanif, T. Wang and J. Shang, *Chem. Eng. J.*, 2019, **370**, 1450–1458.

27 L. Rodriguez-Santiago, M. Sierka, V. Branchadell, M. Sodupe and J. Sauer, *J. Am. Chem. Soc.*, 1998, **120**, 1545–1551.

28 A. Sierraalta, R. Añez and M.-R. Brussin, *J. Phys. Chem. A*, 2002, **106**, 6851–6856.

29 S. Onitsuka, M. Ichiki and T. Watanabe, *US Pat.*, 5158582, 1992.

30 D. Barthomeuf and B.-H. Ha, *J. Chem. Soc., Faraday Trans. 1*, 1973, **69**, 2158–2165.

31 J. Yun and R. Lobo, *Catal. Sci. Technol.*, 2015, **5**, 264–273.

32 P. Hohenberg and W. Kohn, *Phys. Rev.*, 1964, **136**, B864–B871.

33 W. Kohn and L. J. Sham, *Phys. Rev.*, 1965, **140**, A1133–A1138.

34 P. Giannozzi, O. Andreussi, T. Brumme, O. Bunau, M. B. Nardelli, M. Calandra, R. Car, C. Cavazzoni, D. Ceresoli, M. Cococcioni, N. Colonna, I. Carnimeo, A. D. Corso, S. d. Gironcoli, P. Delugas, J. R. A. DiStasio, A. Ferretti, A. Floris, G. Fratesi, G. Fugallo, R. Gebauer, U. Gerstmann, F. Giustino, T. Gorni, J. Jia, M. Kawamura, H. Y. Ko, A. Kokalj, E. Küçükbenli, M. Lazzeri, M. Marsili, N. Marzari, F. Mauri, N. L. Nguyen, H. V. Nguyen, A. Otero-de-la-Roza, L. Paulatto, S. Poncé, D. Rocca, R. Sabatini, B. Santra, M. Schlipf, A. P. Seitsonen, A. Smogunov, I. Timrov, T. Thonhauser, P. Umari, N. Vast, X. Wu and S. Baroni, *J. Phys.: Condens. Matter*, 2017, **29**, 465901.

35 G. Paolo, B. Stefano, B. Nicola, C. Matteo, C. Roberto, C. Carlo, C. Davide, L. C. Guido, C. Matteo, D. Ismaila, C. Andrea Dal, G. Stefano de, F. Stefano, F. Guido, G. Ralph, G. Uwe, G. Christos, K. Anton, L. Michele, M.-S. Layla, M. Nicola, M. Francesco, M. Riccardo, P. Stefano, P. Alfredo, P. Lorenzo, S. Carlo, S. Sandro, S. Gabriele, P. S. Ari, S. Alexander, U. Paolo and M. W. Renata, *J. Phys.: Condens. Matter*, 2009, **21**, 395502.

36 J. P. Perdew, K. Burke and M. Ernzerhof, *Phys. Rev. Lett.*, 1996, **77**, 3865–3868.

37 S. Grimme, *J. Comput. Chem.*, 2006, **27**, 1787–1799.

38 R. Zhang, J.-S. McEwen, M. r. Kollár, F. Gao, Y. Wang, J. Szanyi and C. H. Peden, *ACS Catal.*, 2014, **4**, 4093–4105.

39 Q. Guo, F. Fan, D. Ligthart, G. Li, Z. Feng, E. J. Hensen and C. Li, *ChemCatChem*, 2014, **6**, 634–639.

40 A. G. Greenaway, I. Lezcano-Gonzalez, M. Agote-Aran, E. K. Gibson, Y. Odarchenko and A. M. Beale, *Top. Catal.*, 2018, **61**, 175–182.

41 J. H. Kwak, H. Zhu, J. H. Lee, C. H. Peden and J. Szanyi, *Chem. Commun.*, 2012, **48**, 4758–4760.

42 G. Yalovega, V. Shmatko, A. Funik and M. Brzhezinskaya, *Adv. Mater.*, 2016, 299–315.

43 T. N. Huan, E. S. Andreiadis, J. Heidkamp, P. Simon, E. Derat, S. Cobo, G. Royal, A. Bergmann, P. Strasser and H. Dau, *J. Mater. Chem. A*, 2015, **3**, 3901–3907.

44 N. Shi, Y. Song, X. Xing and J. Chen, *Coord. Chem. Rev.*, 2021, **449**, 214204.

30338 | *J. Mater. Chem. A*, 2024, **12**, 30329–30339

This journal is © The Royal Society of Chemistry 2024

45 M. Sun, C. Ku, Z. Tao, T. Wang, C. Wen, A. Hanif, C. Wang, Q. Gu, P. Sit and J. Shang, *Results Eng.*, 2023, **18**, 101134.

46 C. Bian, D. Li, Q. Liu, S. Zhang, L. Pang, Z. Luo, Y. Guo, Z. Chen and T. Li, *Chin. Chem. Lett.*, 2022, **33**, 1169–1179.

47 R. C. Ambrosio and E. A. Ticianelli, *J. Electroanal. Chem.*, 2005, **574**, 251–260.

48 W. C. Gomes, A. d. O. W. Neto, P. M. Pimentel, D. M. de Araújo Melo and F. R. G. Silva, *Colloids Surf., A*, 2013, **426**, 18–25.

49 F. Delachaux, C. Vallières, H. Monnier and M.-T. Lecler, *Adsorption*, 2019, **25**, 95–103.

50 U. Bentrup, M. Richter and R. Fricke, *Appl. Catal., B*, 2005, **55**, 213–220.

51 A. Mahmood, X. Wang, X. Xie and J. Sun, *Colloids Surf., A*, 2021, **626**, 127058.

52 Z.-M. Wang, T. Arai and M. Kumagai, *Ind. Eng. Chem. Res.*, 2001, **40**, 1864–1871.

53 C. Sedlmair, B. Gil, K. Seshan, A. Jentys and J. A. Lercher, *Phys. Chem. Chem. Phys.*, 2003, **5**, 1897–1905.

54 M. Kantcheva and E. Z. Ciftlikli, *J. Phys. Chem. B*, 2002, **106**, 3941–3949.

55 K. Hadjiivanov, V. Avreyska, D. Klissurski and T. Marinova, *Langmuir*, 2002, **18**, 1619–1625.

56 K. Khivantsev, N. R. Jaegers, H. A. Aleksandrov, L. Kovarik, M. A. Derewinski, Y. Wang, G. N. Vayssilov and J. Szanyi, *Nat. Commun.*, 2021, **12**, 6033.

57 K. I. Hadjiivanov, *Catal. Rev.*, 2000, **42**, 71–144.

This journal is © The Royal Society of Chemistry 2024

J. Mater. Chem. A, 2024, **12**, 30329–30339 | **30339**